



Supporting Information for

Tunable liquid-solid hybrid thermal metamaterials with a topology transition

Peng Jin, Jinrong Liu, Liujun Xu, Jun Wang, Xiaoping Ouyang, Jian-Hua Jiang, and Jiping Huang

Jian-Hua Jiang, Jiping Huang.

E-mail: Jianhuajiang@suda.edu.cn, jphuang@fudan.edu.cn.

This PDF file includes:

Supporting text

Figs. S1 to S9

SI References

Supporting Information Text

Section S1. Basic unit design for independently local control of anisotropic κ and anisotropic σ . In the designed metadevice, the core region (Ω_1) and the background region (Ω_3) are both isotropic, while the shell-like metamaterial region (Ω_2) is anisotropic. To achieve the isotropic thermal properties, we process spherical or cylindrical areas on bulk isotropic solid to fill with water or air. Note that the anisotropic thermal properties are realized by geometric anisotropy. Its component mediums are still isotropic. Fig. S1A shows the effective thermal conductivity of three common solids (Copper, Magnesium alloy, and Inconel alloy) versus their filling fraction of water ϕ_l . Here, we choose Magnesium alloy as the core and the background component and choose Inconel alloy (Copper) as the inclusion (host) of the shell-like metamaterial region. Meanwhile, for processing convenience, the hemispherical part with $R = 5$ mm is hollowed in the type-I unit with a size of $8 \times 8 \times 6$ mm³. Hence, the filling fraction of water ϕ_l is calculated as 0.63, and the effective thermal conductivity of the three solids are marked in Fig. S1A. In the Inconel alloy region, we have both type-I (water-filled) and type-II (air-filled) units. To ensure the same thermal conductivity of these two types of units, the filling fraction of air ϕ_a in the type-II unit is limited to 0.60 (see Fig. S1B). We consider a series of ellipse-embedded structures to achieve the controllable anisotropic thermal conductivity in the shell-like metamaterial region. In each of the above designs, elliptical Inconel alloy ($\kappa = 4$ W m⁻¹ K⁻¹) is placed in the center of the rectangular Copper ($\kappa = 148$ W m⁻¹ K⁻¹), as shown in the lower-right inset of Fig. S1C. We first give a set of values of the major and minor axis of the ellipses. With the aid of accurate finite-element simulations, we get the steady-state averaged amplitude of total heat flux (and temperature gradient) in the direction of heat transport in the whole simulation box (30×30.5 mm²) of the inset. Therefore, the ratio of the former to the latter is the effective thermal conductivity in the direction of heat transport. Through tuning the major and minor axis of the ellipses, we realize the local control of anisotropic thermal conductivity in the ellipse-embedded structure (see Fig. S1C). In the designed metadevice, we choose the size of the semi-minor axis a as 13 mm, the semi-major axis b as 15 mm, and the type-II unit (see lower-right inset in Fig. S1D) as 25×5 mm². Meanwhile, we set the permeability of the type-II unit as 10^{-18} m² because parameters cannot be set to zero in finite-element simulations. The permeability of the type-I units is set as 2.68×10^{-9} m², see “Experimental Section” in the main text. Using the same accurate finite-element simulations as above (changing total heat flux to fluid velocity; changing temperature gradient to pressure gradient; results multiplied by dynamic viscosity 0.001 Pa · s), the dependence of effective anisotropic permeability in the ellipse-embedded structure on the orientation of the type-II unit (θ_0 in the inset of Fig. S1D) is illustrated in Fig. S1D. Note that the permeability can still be tuned independently when the thermal conductivity is determined. Finally, we realize the independently local control of anisotropic thermal conductivity κ and anisotropic permeability σ .

Section S2. Proof of form-invariance of governing equations and transformation rules of relevant dominant parameters. For realization of thermal cloaking, the governing equation of Eq. (2) in the main text could be simplified to

$$\nabla \cdot (\kappa \cdot \nabla T) = 0, \quad [S1]$$

when the pressure difference of the system (ΔP) equals to zero. First, we prove the form-invariance of Eq. (S1) after realizing the space transformation from a curvilinear space K to a physical space K' . The space transformation is determined by the Jacobian transformation matrix Ξ . Let's rewrite the composition of Eq. (S1). In the curvilinear space K , the set of contravariant basis is expressed as $(\mathbf{g}^i, \mathbf{g}^j, \mathbf{g}^k)$ and corresponding contravariant components are (x^i, x^j, x^k) . Eq. (S1) could be rewritten as

$$\begin{aligned} \nabla \cdot (\kappa \cdot \nabla T) &= \frac{\partial}{\partial x^i} \left(\kappa^{ij} \frac{\partial T}{\partial x^j} \right) + \Gamma_{ki}^k \left(\kappa^{ij} \frac{\partial T}{\partial x^j} \right) \\ &= \frac{1}{\sqrt{g}} \partial_i \left(\sqrt{g} \kappa^{ij} \partial_j T \right), \end{aligned} \quad [S2]$$

where g is the determinant of $\mathbf{g}_i \cdot \mathbf{g}_j$. Here, $(\mathbf{g}_i, \mathbf{g}_j, \mathbf{g}_k)$ is the set of covariant basis. The Christoffel symbol is $\Gamma_{ki}^j = (\partial_k \mathbf{g}_i) \cdot \mathbf{g}^j$, thus leading to $\Gamma_{ki}^k = \partial \sqrt{g} / (\sqrt{g} \partial x^i)$. So far, the form-invariance of Eq. (S1) has been proved. Next, we should rewrite Eq. (S1) in the physical space K' for the transformation rules of material properties, performed in the Cartesian coordinate system $(x^{i'}, x^{j'}, x^{k'})$,

$$\partial_{i'} \frac{\partial x^{i'}}{\partial x^i} \left[\sqrt{g} \left(\kappa^{ij} \frac{\partial x^{j'}}{\partial x^j} \partial_{j'} T \right) \right] = 0, \quad [S3]$$

where $\partial x^{i'}/\partial x^i$ and $\partial x^{j'}/\partial x^j$ are the components of the Jacobian transformation matrix Ξ , and $\sqrt{g} = 1/\det \Xi$. We change space transformation into material transformation,

$$\partial_{i'} \left(\frac{\frac{\partial x^{i'}}{\partial x^i} \kappa^{ij} \frac{\partial x^{j'}}{\partial x^j}}{\det \Xi} \partial_{j'} T \right) = 0. \quad [S4]$$

Thus, we get the transformation rule as

$$\kappa' = \Xi \kappa \Xi^T / \det \Xi. \quad [S5]$$

The space transformation of cloaking need compress a circular region ($r < R_1$) from the central region into a shell ($R_1 < r < R_2$), which means

$$\begin{cases} r' = (R_2 - R_1) r / R_2 + R_1, & 0 < r < R_2 \\ \theta' = \theta. \end{cases} \quad [S6]$$

The Jacobian transformation matrix $\boldsymbol{\Xi}$ is calculated by

$$\boldsymbol{\Xi} = \begin{pmatrix} \partial r' / \partial r & \partial r' / (r \partial \theta) \\ r' \partial \theta' / \partial r & r' \partial \theta' / (r \partial \theta) \end{pmatrix}. \quad [\text{S7}]$$

Considering an isotropic medium with thermal conductivity of κ in the curvilinear space K , the thermal conductivity κ' in the physical space K' for cloaking is calculated as

$$\kappa' = \begin{pmatrix} 1 - R_1/r' & 0 \\ 0 & -r'/ (R_1 - r') \end{pmatrix} \kappa. \quad R_1 < r' < R_2 \quad [\text{S8}]$$

In convenience of practical preparation, we propose an approximately r -independent structures for cloaking. The related space transformation is

$$\begin{cases} r' = R_1 r / R_m, & 0 < r < R_m \\ r' = R_2 (r/R_2)^M, & R_m < r < R_2 \\ \theta' = \theta, \end{cases} \quad [\text{S9}]$$

where $M < 1$ is nonlinear order of the approximate space transformation for cloaking and $R_m = R_2 (R_1/R_2)^{1/M}$ determines the cloaking ratio (the closer to zero, the better the approximation). In this case, the thermal conductivity κ' is

$$\begin{cases} \kappa' = \begin{pmatrix} 1 & 0 \\ 0 & 1 \end{pmatrix} \kappa, & 0 < r' < R_1 \\ \kappa' = \begin{pmatrix} M & 0 \\ 0 & 1/M \end{pmatrix} \kappa. & R_1 < r' < R_2 \end{cases} \quad [\text{S10}]$$

When the pressure difference (ΔP) is large enough, there is only convective heat flux in the total heat flux. The governing equation of Eq. (2) could be simplified to

$$\nabla \cdot (\rho C \mathbf{v} T) = 0. \quad [\text{S11}]$$

Similarly, the convective term can be written in the curvilinear space K as

$$\begin{aligned} \nabla \cdot (\rho C \mathbf{v} T) &= \frac{\partial}{\partial x^i} (\rho C v^i T) + \Gamma_{ki}^k (v^i T) \\ &= \frac{1}{\sqrt{g}} \partial_i (\sqrt{g} \rho C v^i T), \end{aligned} \quad [\text{S12}]$$

where \mathbf{v} is denoted as $\mathbf{v} = -\sigma/\eta \nabla P$. We have proved the form-invariance of Eq. (S11). For the transformation rules of material properties, Eq. (S11) should be rewritten in the physical space K' as

$$\partial_{i'} \frac{\partial x^{i'}}{\partial x^i} (\sqrt{g} \rho C v^i T) = 0, \quad [\text{S13}]$$

Changing space transformation into material transformation, we get

$$\partial_{i'} \left(\rho C \frac{\partial x^{i'}}{\partial x^i} v^i T \right) = 0. \quad [\text{S14}]$$

Thus, the transformation rule could be expressed as

$$\mathbf{v}' = \boldsymbol{\Lambda} \mathbf{v} / \det \boldsymbol{\Lambda}. \quad [\text{S15}]$$

When considering steady-state creeping flow in porous media, the transformation rule further becomes

$$\boldsymbol{\sigma}' = \boldsymbol{\Lambda} \boldsymbol{\sigma} \boldsymbol{\Lambda}^T / \det \boldsymbol{\Lambda}. \quad [\text{S16}]$$

The space transformation of concentration need two steps. The first step is to compress a larger circular region ($R < R_m$) into a smaller one ($R < R_1$). The second step is to stretch the smaller shell ($R_m < R < R_2$) into the larger one ($R_1 < R < R_2$). Above two steps are concluded as

$$\begin{cases} r' = R_1 r / R_m, & 0 < r < R_m \\ r' = [(R_1 - R_m) R_2 + (R_2 - R_1) r] / (R_2 - R_m), & R_m < r < R_2 \\ \theta' = \theta, \end{cases} \quad [\text{S17}]$$

where R_m determines the concentration ratio. The Jacobian transformation matrix $\boldsymbol{\Lambda}$ is calculated by

$$\boldsymbol{\Lambda} = \begin{pmatrix} \partial r' / \partial r & \partial r' / (r \partial \theta) \\ r' \partial \theta' / \partial r & r' \partial \theta' / (r \partial \theta) \end{pmatrix}. \quad [\text{S18}]$$

Also, there exists an isotropic medium with permeability of σ in the curvilinear space K . The permeability σ' in the physical space K' for concentration is

$$\begin{cases} \sigma' = \begin{pmatrix} 1 & 0 \\ 0 & 1 \end{pmatrix} \sigma, & 0 < r' < R_1 \\ \sigma' = \begin{pmatrix} \frac{-R_1 R_2 - R_m r' + R_2 (R_m + r')}{r'(R_2 - R_m)} & 0 \\ 0 & \frac{r'(R_2 - R_m)}{-R_1 R_2 - R_m r' + R_2 (R_m + r')} \end{pmatrix} \sigma, & R_1 < r' < R_2 \end{cases} \quad [\text{S19}]$$

In convenience of practical preparation, we propose an approximately r -independent structures for concentration. The related space transformation is

$$\begin{cases} r' = R_1 r / R_m, & 0 < r < R_m \\ r' = R_2 (r / R_2)^N, & R_m < r < R_2 \\ \theta' = \theta, \end{cases} \quad [\text{S20}]$$

where $N > 1$ is nonlinear order of the approximate space transformation for concentration and R_m takes $R_m = R_2 (R_1 / R_2)^{\frac{1}{N}}$ (the closer to R_2 , the better the approximation). In this case, the permeability σ' is

$$\begin{cases} \sigma' = \begin{pmatrix} 1 & 0 \\ 0 & 1 \end{pmatrix} \sigma, & 0 < r' < R_1 \\ \sigma' = \begin{pmatrix} N & 0 \\ 0 & 1/N \end{pmatrix} \sigma, & R_1 < r' < R_2 \end{cases} \quad [\text{S21}]$$

In part “Simulation and characterization” of the main text, we choose the nonlinear order $M = 0.1$ of approximate space transformation for cloaking and $N = 10$ for concentration. Fig. S2 shows the comparison of exact and approximate space transformation for cloaking and concentration, respectively.

Section S3. Simulations of liquid flow profiles in the main text. When local thermal equilibrium is reached everywhere, the heat flow must be stable, and the liquid flow should be. In the main text, we have shown from finite-element simulations the heat flow characteristics of different thermal functions of the metadevice. The results of relevant liquid features, which demonstrate the realization of fluid concentration, are shown in Figs. S3A-F. The pressure (color) and the fluid velocity (color and vectors) profiles are presented in these figures. As anticipated, with the increase of external hydraulic pressure ΔP , the fluid velocity in the whole metadevice is increasing, and the liquid flow always maintains the effect of concentration. Fig. S3G presents the averaged product of fluid velocity and temperature in the core region as functions of the external hydraulic pressure. To find a more convenient factor to characterize thermal concentration, the ratio of three quantities related to thermal convection in our metadevice and the reference are calculated in the range of external hydraulic pressure 750 Pa to 1000 Pa. Three quantities are the averaged amplitude of the convective heat flux, the product of the fluid velocity and temperature, and the fluid velocity in the core region. As shown in the inset of Fig. S3G, these three ratios give an excellent approximation effect to β_{\max} with external hydraulic pressure increasing to 1000 Pa. The above results provide a valuable guide for convenient experimental characterization of thermal concentration.

Section S4. Theoretical derivation and discussions of β_{\max} . In the main text, we mention that when the pressure difference (ΔP) of the whole system is very large, the temperature of the system evolves into the temperature of the hot reservoir. There is only convective heat flow (\mathbf{J}_{conv}) in the system. Thus, the maximum value of β can be calculated as

$$\beta_{\max} = \frac{\rho C v T_h}{\rho C v_0 T_h} = \frac{-\rho C \frac{\sigma_1}{\eta} |\nabla P_1| T_h}{-\rho C \frac{\sigma_1}{\eta} |\nabla P_0| T_h} = \frac{|\nabla P_1|}{|\nabla P_0|}, \quad [\text{S22}]$$

where $|\nabla P_0|$ is the modulus of the external linear pressure field $\Delta P / L$ in the reference. $|\nabla P_1|$ is the gradient of the pressure in the x direction in Ω_1 of the metadevice from the Laplace equation (1), expressed by

$$|\nabla P_1| = \frac{-4R_1^{m_1-1} R_2^{m_1+1} m_1 \frac{\sigma_{rr}}{\eta} \frac{\sigma_3}{\eta} |\nabla P_0|}{R_1^{2m_1} \left(-\frac{\sigma_1}{\eta} + m_1 \frac{\sigma_{rr}}{\eta} \right) \left(m_1 \frac{\sigma_{rr}}{\eta} - \frac{\sigma_3}{\eta} \right) - R_2^{2m_1} \left(\frac{\sigma_1}{\eta} + m_1 \frac{\sigma_{rr}}{\eta} \right) \left(m_1 \frac{\sigma_{rr}}{\eta} + \frac{\sigma_3}{\eta} \right)}, \quad [\text{S23}]$$

where m_1 is $\sqrt{\frac{\sigma_{\theta\theta}}{\sigma_{rr}}}$. Considering $\sigma_1^2 = \sigma_{rr} \sigma_{\theta\theta}$ for concentration of convective flux and $\sigma_3 = \sigma_1$, β_{\max} could be further reduced as

$$\begin{aligned} \beta_{\max} &= \frac{-4R_1^{m_1-1} R_2^{m_1+1} m_1 \frac{\sigma_{rr}}{\eta} \frac{\sigma_3}{\eta}}{R_1^{2m_1} \left(-\frac{\sigma_1}{\eta} + m_1 \frac{\sigma_{rr}}{\eta} \right) \left(m_1 \frac{\sigma_{rr}}{\eta} - \frac{\sigma_3}{\eta} \right) - R_2^{2m_1} \left(\frac{\sigma_1}{\eta} + m_1 \frac{\sigma_{rr}}{\eta} \right) \left(m_1 \frac{\sigma_{rr}}{\eta} + \frac{\sigma_3}{\eta} \right)} \\ &= \left(\frac{R_2}{R_1} \right)^{1 - \frac{\sigma_1}{\sigma_{rr}}}. \end{aligned} \quad [\text{S24}]$$

To prove the correctness of Eq. (S23), we provide the simulated results $|\nabla P_1|$ of metadevices with three degrees of permeability anisotropy, as shown in Figs. S4A-C. The ratio between the average $|\nabla P_1|$ and the theoretical results from

Eq. (S23) in the above three cases are 0.89, 0.89, and 0.89, respectively. So the simulated results $|\nabla P_1|$ are in good agreement with the results from Eq. (S23).

We emphasize that the tunability of the thermal metadevice and its function are due to the controllable thermal convection associated with the fluid flows as tuned by the external hydraulic pressure. Theoretically, there is an upper bound for the heat amplification factor β_{\max} which depends on R_2/R_1 and σ_{rr}/σ_1 , as given in Eq. (S24). This upper bound, β_{\max} , is reached when the heat flux in the core region is dominated by thermal convection. We illustrate the dependence of β on the external hydraulic pressure for various parameters in the upper part of Fig. S5A where metashells with three different geometries, $R_2/R_1 = 1.6, 3.2$, and 5 ($R_1 = 0.02$ mm is fixed), are first studied. The heat amplification factor increases with the external hydraulic pressure for all three cases. However, they reach different maximum values under large hydraulic pressures, reflecting distinct β_{\max} . In accordance with Eq. (S24), β_{\max} increases with the R_2/R_1 , which indicates that the tunability of the devices with larger R_2/R_1 is more significant. This result is consistent with the picture that thermal transport manipulations are achieved in the region Ω_2 , which has a larger effect when it has a larger area.

The maximum heat amplification factor β_{\max} also depends on the permeability anisotropy σ_{rr}/σ_1 , given from Eq. (S24). Therefore, we then illustrate the dependence of β on the external hydraulic pressure ΔP for three different permeability anisotropy, $\sigma_{rr}/\sigma_1 = 10, 50$, and 100 ($\sigma_1 = 10^{-12}$ m 2 is fixed). As shown in lower part of Fig. S5A, three cases of β increase with the external hydraulic pressure ΔP . Also, β_{\max} can be enhanced ($\beta_{3,\max} > \beta_{2,\max} > \beta_{1,\max}$) by increasing the degree of permeability anisotropy, consistent with Eq. (S24). From a physical point of view, larger permeability allows bigger flow in the core region, making a bigger convective heat flux than that in the background. Fig. S5B shows the dependence of the maximum heat amplification factor β_{\max} on both geometry R_2/R_1 and the permeability anisotropy σ_{rr}/σ_1 . Clearly, β_{\max} from finite-element simulation results of Fig. S5A are consistent with results from Eq. (S24), which confirms the reliability of the theoretical derivation of β_{\max} .

Section S5. Topological switch from concentration to cloaking in liquid-solid hybrid thermal metamaterials. Fig. S6 shows a metadevice in a two-dimensional system, which can realize a topological switch from concentration to cloaking with the increase of external hydraulic pressure. Finite-element simulations (Fig. S7) are performed to verify this effect. The simulation box is 0.1×0.1 mm 2 with $R_1 = 0.02$ mm and $R_2 = 0.032$ mm, whose outlines are all marked with solid black lines in Figs. S7B-G. The homogeneous background and the core region have the same parameters: the isotropic thermal conductivity $\kappa_1 = 1$ W m $^{-1}$ K $^{-1}$ and the isotropic liquid permeability $\sigma_1 = 10^{-12}$ m 2 . The metashell is parameterized for concentration conductive heat flux, with $\kappa_2 = \text{diag}(10, 0.1)$ W m $^{-1}$ K $^{-1}$, and cloaking convective heat flux, with $\sigma_2 = \text{diag}(0.1, 10) \times 10^{-12}$ m 2 . The reference is the homogeneous background with the same simulation box. The averaged amplitude of total heat flux (J_{tot}) in the core region (Ω_1) is recorded as the external hydraulic pressure (ΔP) is increased from 0 to 1000 Pa at intervals of 10 Pa, as shown in the inset of Fig. S7A. The solid line and dashed lines are the metadevice and the reference results, respectively. The ratio of the former and the latter is the dependence of the heat flow amplification factor (β) on ΔP , as shown in Fig. S7A. In Fig. S7B, when $\Delta P = 0$ Pa, there is no convective heat flux (J_{conv}) in the whole system. The thermal conductivity (concentration-effect) dominates the total heat flux, flowing furthest into the core region. At this point, β is 1.527. When ΔP is 202.4 Pa [see Figs. S7C and F], the averaged amplitude of total heat flux in the core region is consistent with that in the reference ($\beta = 1.000$). When ΔP is extremely high ($\Delta P = 1000$ Pa) [see Fig. S7D], the convective heat flux (J_{conv}) accounts for a large proportion of the total heat flux in the whole system. The distribution of total heat flux is dominated by the permeability (cloaking effect), bypassing the core region. β is 0.082, close to 0. However, convective heat flux does not completely suppress conductive heat flux in the core region, and the concentration effect of the original conductive heat flux in the core region is slightly retained. At this time, the averaged amplitude of total heat flux in the core region for the reference is so large that the influence of the conductive heat flux in the core region [see Fig. S7D] can be ignored. Essentially, the results in Fig. S7H are similar to those in Fig. S5B; that is, the minimum value of β can be weakened by increasing the degree of permeability anisotropy σ_1/σ_{rr} or decreasing R_2/R_1 . Fig. S7I summarizes the variations in the averaged amplitude of J_{conv} , J_{cond} , J_{tot} in the core region with ΔP of the reference (subscript: 0) and the metadevice (subscript: 1). In the case of the metadevice, the averaged amplitude of convective heat flux ($J_{1,\text{conv}}$) in the core region increases with the increase of ΔP , while the averaged amplitude of conductive heat flux ($J_{1,\text{cond}}$) in the core region decreases with the increase of ΔP . These results indicate convective heat flux accounts for a large proportion of the total heat flux at a large ΔP . Thus, a proposed liquid-solid hybrid thermal metamaterial presents a virtual space topological switch from concentration to cloaking induced by external hydraulic pressure.

Section S6. Steady-state finite-element simulation results of the sample. To further illustrate the reliability of the experimental results, we also perform finite-element simulations based on the designed sample. As initialization, Darcy's law and porous media heat transfer modules are used in the two-dimensional steady-state models. The simulation box is 300×300 mm 2 , and other parameters are the same as those of the actual experimental sample in the $x - y$ plane. For cloaking validation ($\Delta P = 0$ Pa), we set the upper and lower boundaries of the system as adiabatic conditions. When the left and right ends of the system are set as high and low temperatures (line heat source), temperature, conductive heat flux, and total heat flux profiles of the designed sample are calculated, as shown in Figs. S8A-C. It can be observed from Fig. S8A that the white isotherms of the background are not curved, and the color in the core region is uniform, showing a well-cloaking effect. When it comes to concentration validation, we first set the permeability for the two-dimensional model in finite-element simulations. For each black dashed box inside of Fig. 3C, we set the permeability as 10^{-18} m 2 . For other regions, the permeability is 2.68×10^{-9} m 2 . We set the temperature (external hydraulic pressure) at left and right boundaries as 343 K and 283 K (1000 Pa and 0 Pa) and obtain finite-element simulation results when the system is stable (see Figs. S8D-I). Notably, the temperature of the whole

system is the temperature of the left boundary (Fig. S8D). Fig. S8F displays that the fluid velocity in the core region is more significant than that in the background. The above results are consistent with experimental results in Fig. 3E. Moreover, Fig. S8G also shows a concentration effect driven by external hydraulic pressure.

Section S7. Application for thermal illusion and camouflage of our metadevice. Suppose we place an object with the same permeability and thermal conductivity as the background material in the core region. For thermal illusion, we can adjust the external hydraulic pressure, switch the object's temperature in the core region, and realize the temperature illusion of the object in the core region; see the simulation results in Figs. 2B-D. For thermal camouflage, we consider the simulation result in Fig. 2D. No matter where we put the object in the core region, the temperature of the core region is still the temperature of the hot source. Only from the temperature distributions the exact position of the object cannot be found, so our metadevice has realized the function of thermal camouflage.

Section S8. Analyzation of the small change of effective T_c in the experiment from heat exchange of the cold boundary. When we increase the velocity v by changing the external hydraulic pressure ΔP , the total heat flux $J_{0,tot}(\Delta P)$ increase $\delta J \propto (vT - \lambda\kappa\delta T_c)$, and the temperature of cold boundary T_c increase $\delta T_c \propto \delta J/h$, where \propto means proportional, λ is a ratio determined by materials and structure, κ is thermal conductivity of the system, and h is the convection coefficient. Therefore, introducing the heat exchange boundary is equivalent to a decrease of $\Delta T = T_h - T_c$ and thus promotes the pushed-right temperature distribution.

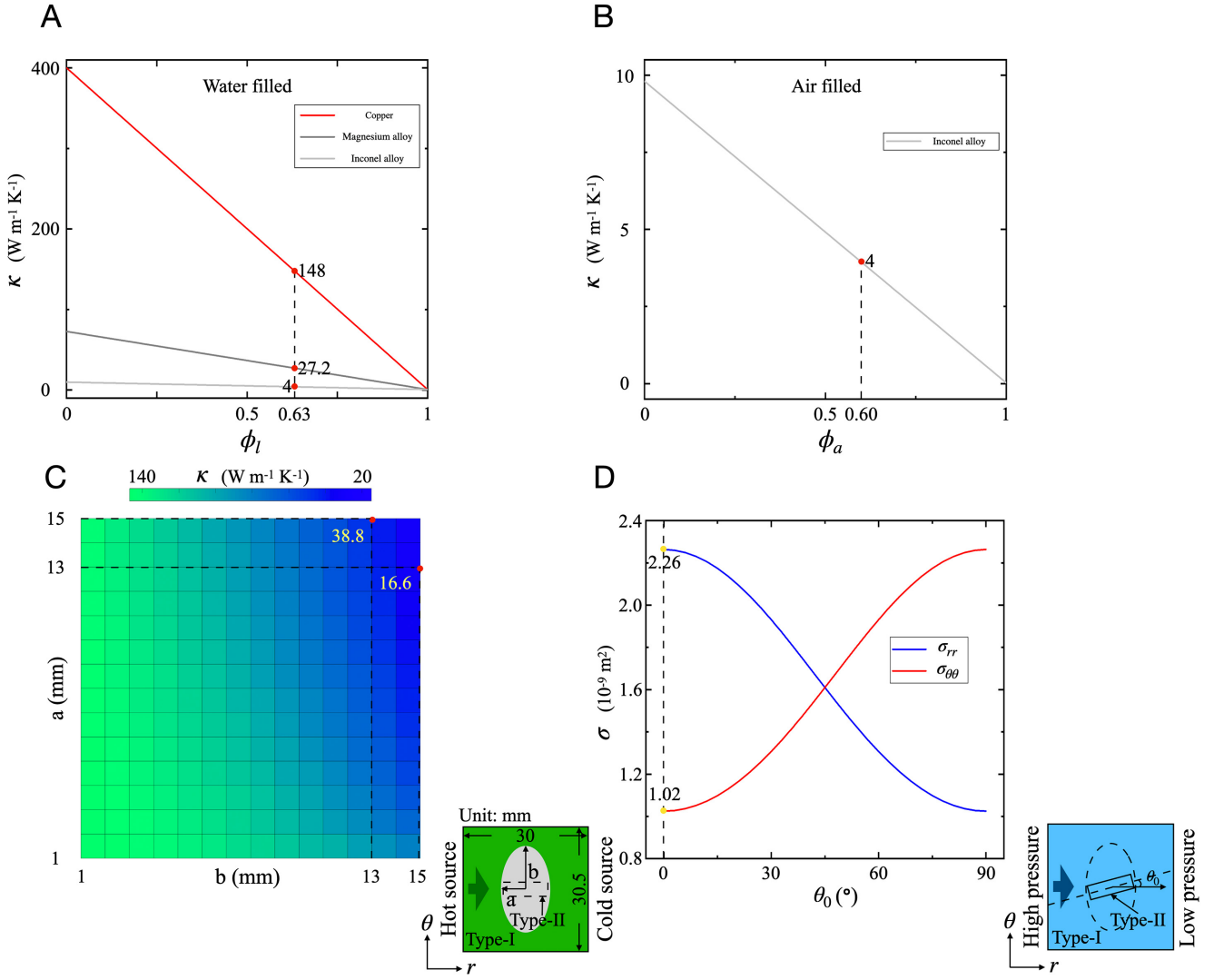


Fig. S1. Local control over κ and σ via basic units design. (A) κ of isotropic medium (type-I unit) which made of three solids (Copper, Magnesium alloy, and Inconel alloy) and liquid (Water) versus filling fraction ϕ_l . (B) κ of isotropic medium (type-II unit) which made of solid (Inconel alloy) and air versus filling fraction ϕ_a . (C) κ of anisotropic medium (elliptic Inconel alloy embedded in Copper) versus the semi-minor axis a and semi-major axis b of the ellipse. In the lower-right inset, outside the rectangular dashed box is type-I unit, while inside is type-II unit. (D) σ of anisotropic medium (type-II unit placed in the center of type-I unit) versus the orientation of type-II unit (θ_0 from the lower-right inset).

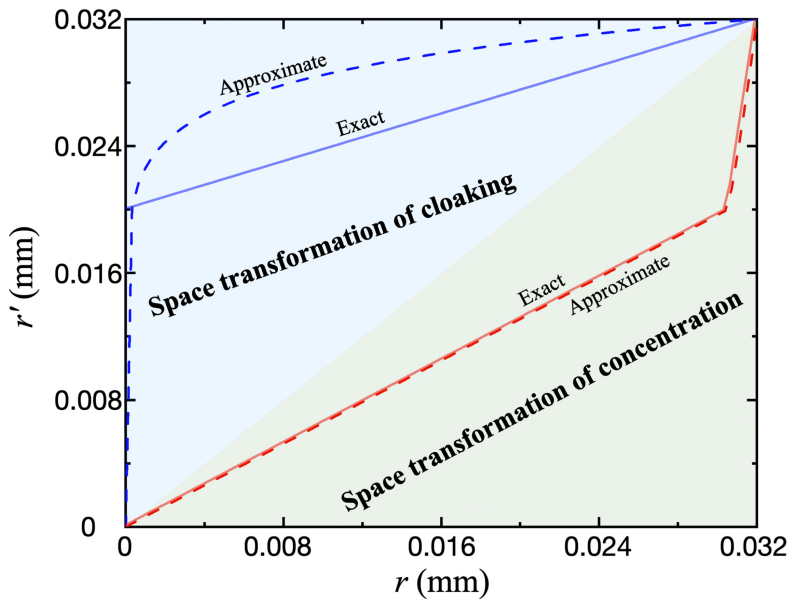


Fig. S2. Exact and approximate space transformation of cloaking and concentration for case of finite-element simulations in the main text.

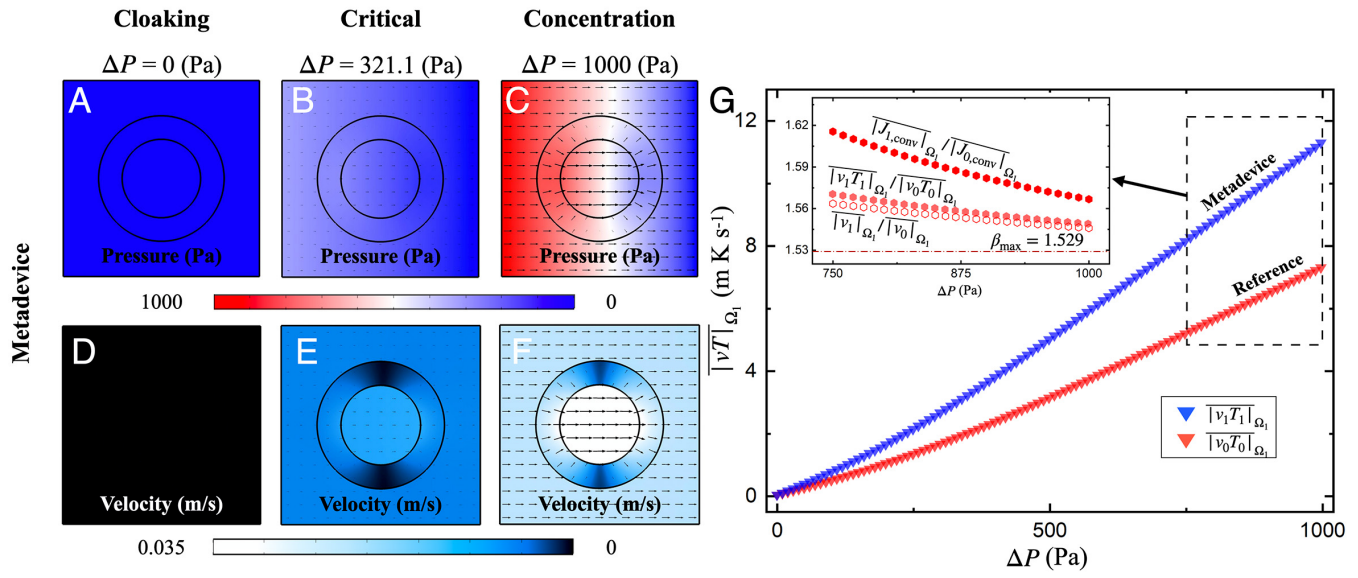


Fig. S3. Simulations of liquid flow profiles in the main text. (A-C) Pressure (color) and fluid velocity (vectors) profiles in the metadevice with $\Delta P = 0, 321.1, 1000$ Pa, respectively. (D-F) Fluid velocity (color and vectors) profiles in the metadevice with $\Delta P = 0, 321.1, 1000$ Pa, respectively. (G) Averaged amplitude of product of the fluid velocity and the temperature in the core region as functions of ΔP of the metadevice and the reference. The inset shows the ratio of the averaged amplitude of convective heat flux, product of the fluid velocity and the temperature, fluid velocity in the core region in the metadevice and the reference.

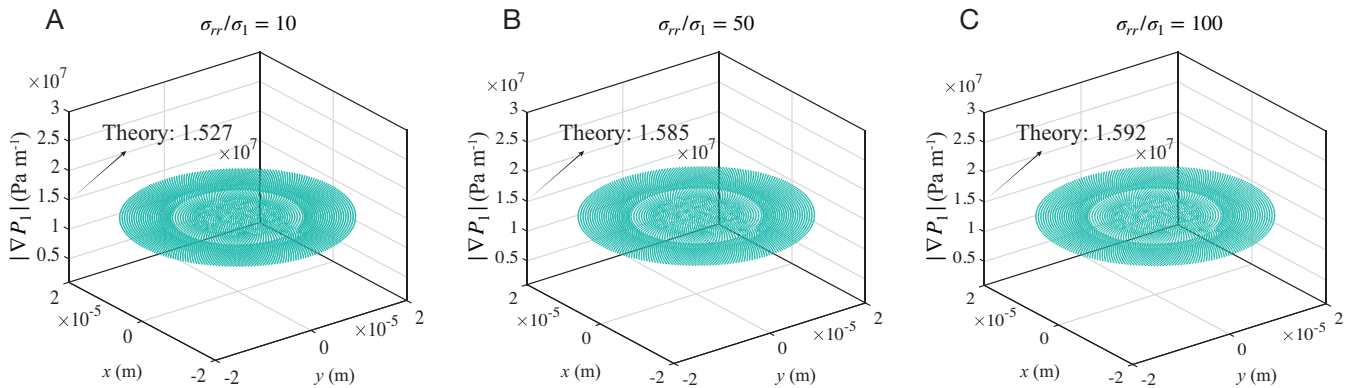


Fig. S4. (A - C) Simulated results $|\nabla P_1|$ of metadevices with three degrees of permeability anisotropy, $\sigma_{rr}/\sigma_1 = 10, 50$, and 100 ($\sigma_1 = 10^{-12} \text{ m}^2$ is fixed). Other parameters are the same as those in Fig. 2D.

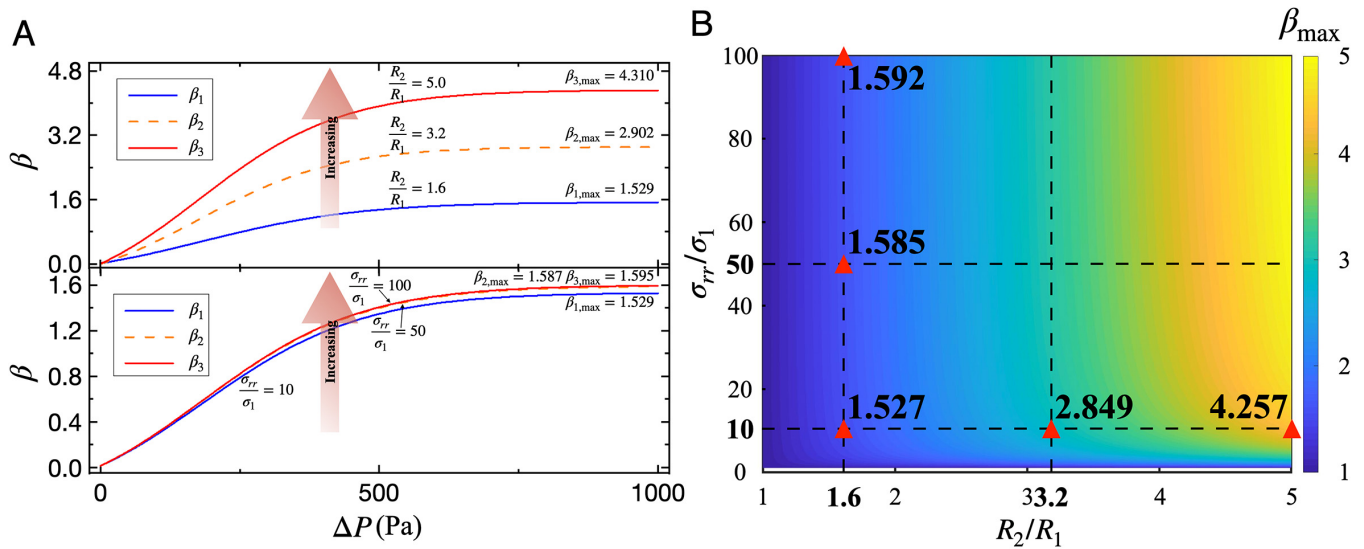


Fig. S5. Upper part of (A) Relationship between β and ΔP for three different geometries, $R_2/R_1 = 1.6, 3.2$, and 5 ($R_1 = 0.02$ mm is fixed). Subscript: 1, 2, and 3. Lower part of (A) Relationship between β and ΔP for three degrees of permeability anisotropy, $\sigma_{rr}/\sigma_1 = 10, 50$, and 100 ($\sigma_1 = 10^{-12}$ m 2 is fixed). Subscript: 1, 2, and 3. (B) The dependence of the maximum heat amplification factor β_{\max} on both geometry R_2/R_1 and degree of permeability anisotropy σ_{rr}/σ_1 .

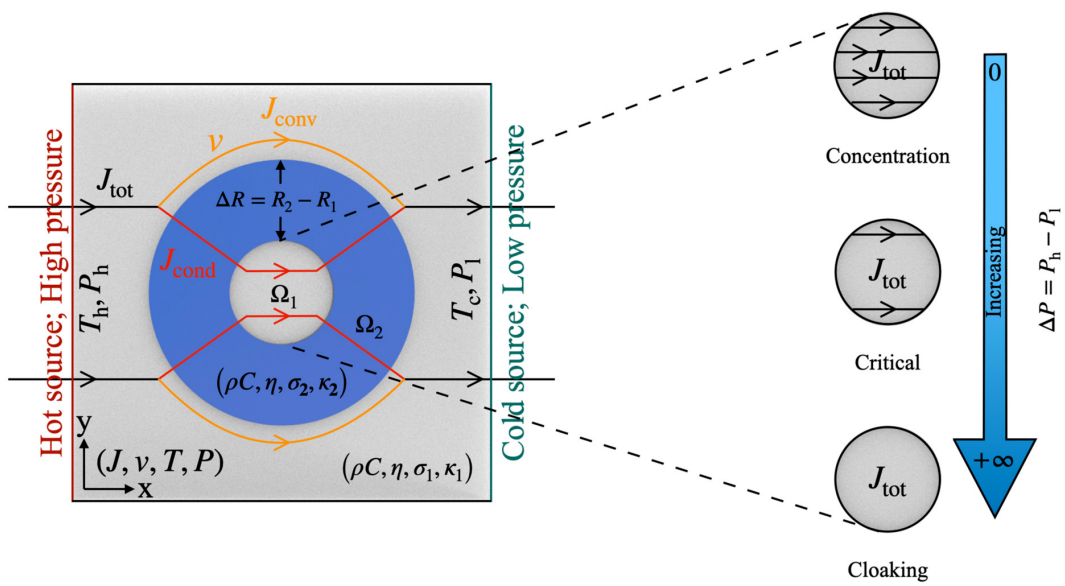


Fig. S6. Metadevice in a two-dimensional system for concentration conductive flux and cloaking convective flux.

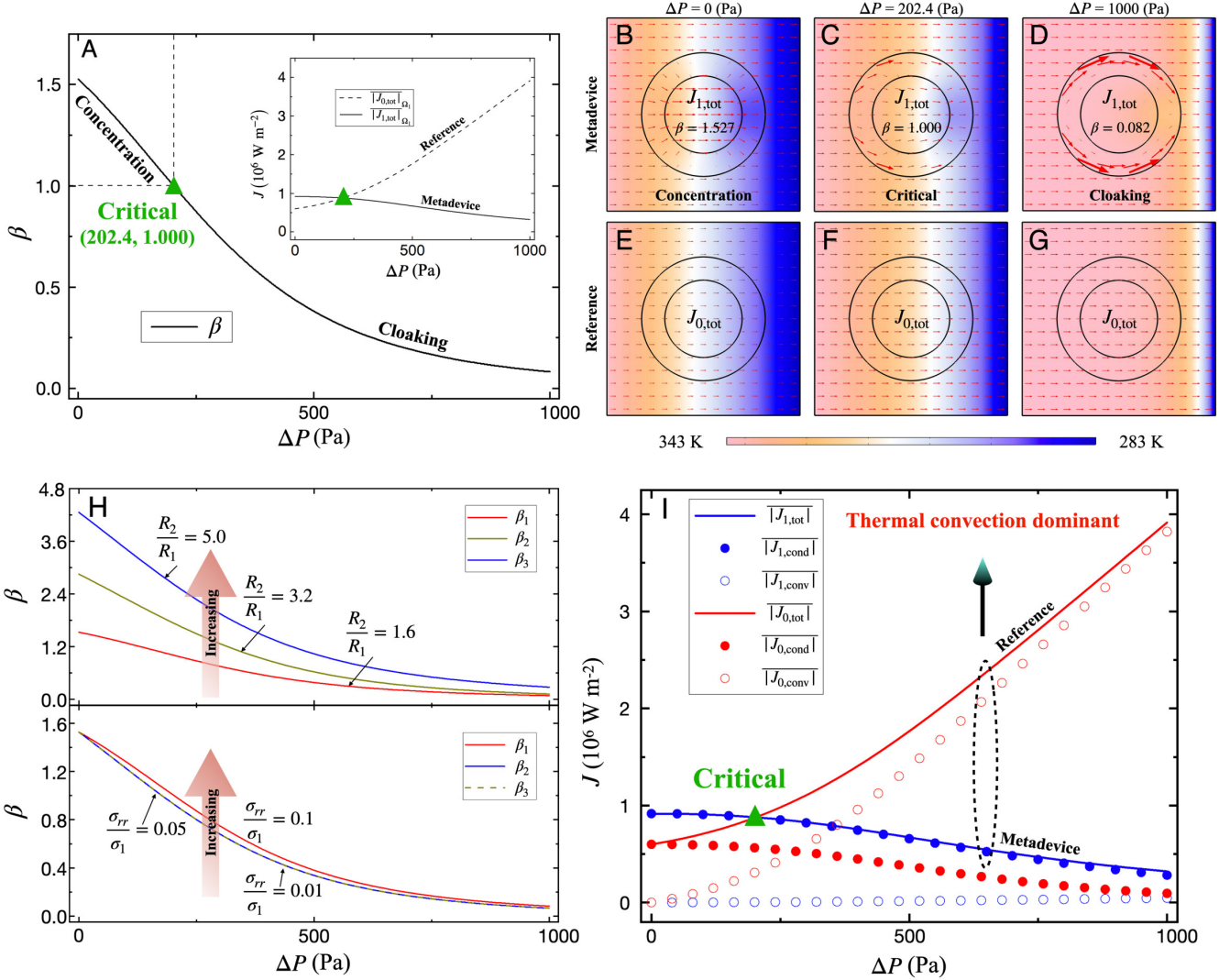


Fig. S7. Results of numerical and finite-element simulations. (A) Evolution of the heat flux amplification factor β with the external hydraulic pressure difference ΔP . The inset shows the dependence of the averaged amplitude of the total heat flux (J_{tot}) in the core region on the pressure difference ΔP . The solid and dashed lines represent the heat fluxes for the metadevice (subscript 1) and the reference (subscript 0), respectively. (B-D) Temperature (color) and heat flux (vectors) profiles in the metadevice with $\Delta P = 0$, 202.4, 1000 Pa. (E-G) Temperature (color) and heat flux (vectors) profiles in the reference with $\Delta P = 0$, 202.4, 1000 Pa. Upper part of (H) Relationship between β and ΔP for three different geometries, $R_2/R_1 = 1.6, 3.2$, and 5 ($R_1 = 0.02 \text{ mm}$ is fixed). Lower part of (H) Relationship between β and ΔP for three degrees of permeability anisotropy, $\sigma_{rr}/\sigma_1 = 0.1, 0.05$, and 0.01 ($\sigma_1 = 10^{-12} \text{ m}^2$ is fixed). Subscript: 1, 2, and 3. (I) The averaged amplitude of the convective (J_{conv}), conductive (J_{cond}), and total (J_{tot}) heat fluxes in the core region for metadevice and reference as functions of the ΔP .

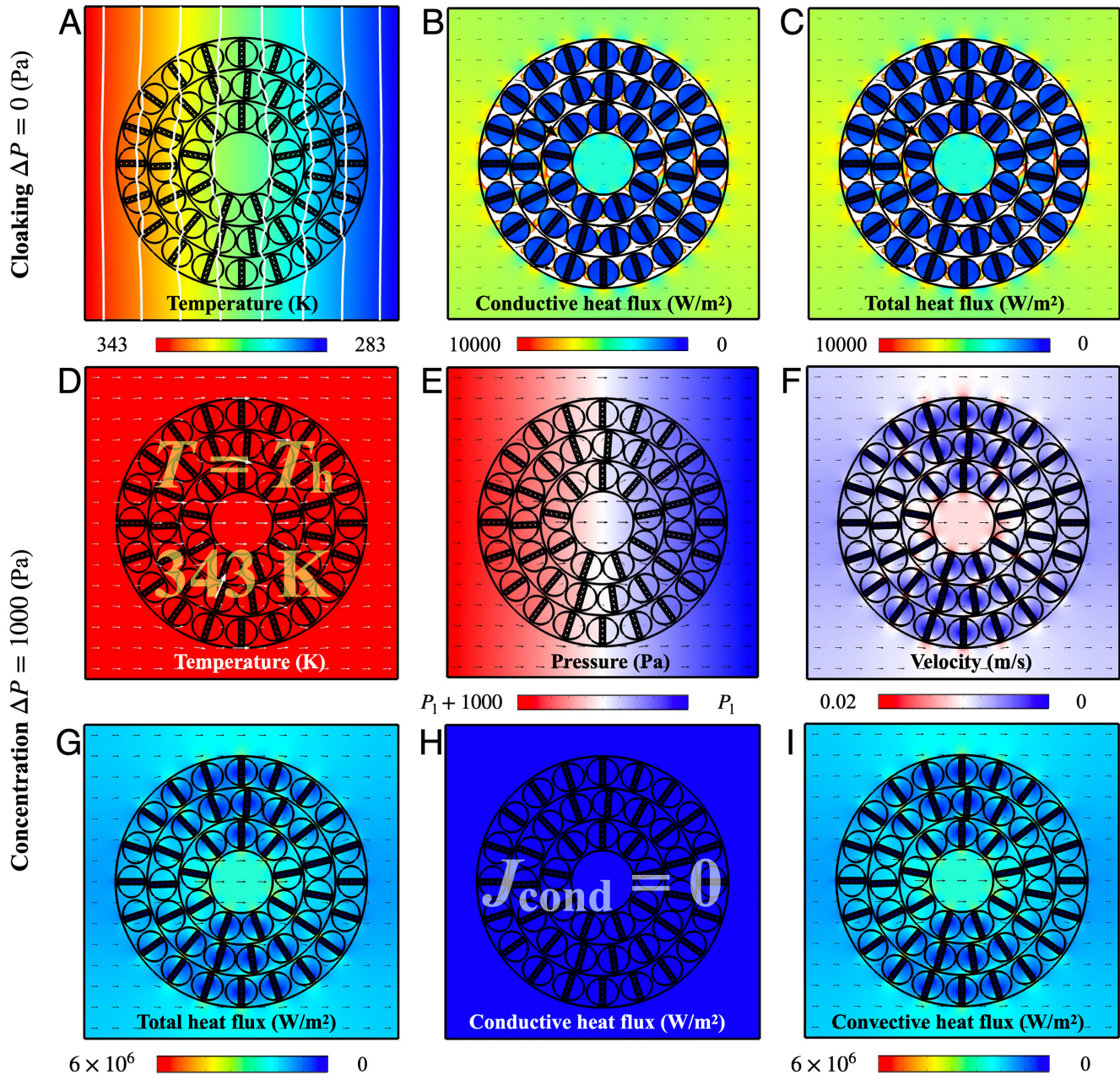


Fig. S8. Finite-element simulation results of the designed sample. (A-C) Temperature (color), conductive heat flux (color and vectors), and total heat flux (color and vectors) profiles of the designed sample with $\Delta P = 0$ Pa, respectively. (D) Temperature (color) profiles of the designed sample with $\Delta P = 1000$ Pa. The vectors represent the total heat flux distributions. (E) and (F) Pressure (color) and fluid velocity (color) profiles of the designed sample when external hydraulic pressure $\Delta P = 1000$ Pa, respectively. The vectors represent the velocity profiles. (G-I) Total heat flux (color and vectors), conductive heat flux (color and vectors), convective heat flux (color and vectors) profiles of the designed sample when external hydraulic pressure $\Delta P = 1000$ Pa, respectively.

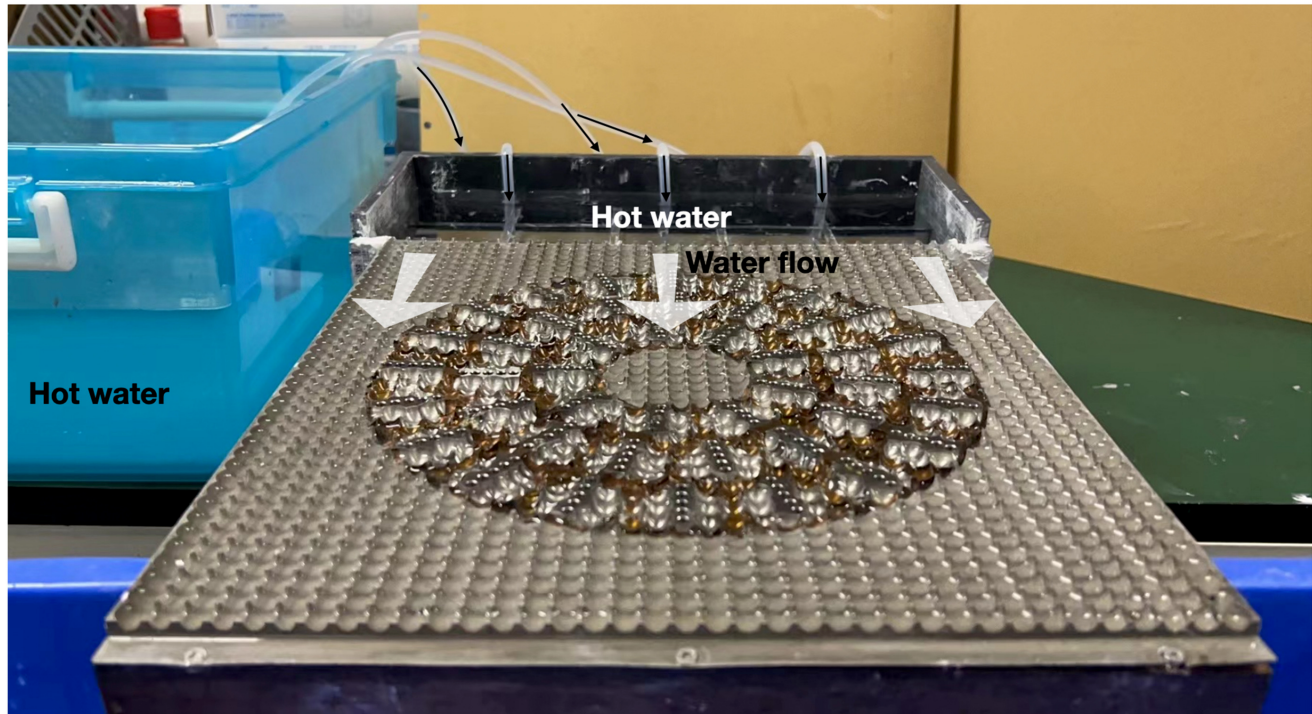


Fig. S9. The real experimental setup to verify concentration performance.

References

1. L. Xu, S. Yang, J. Huang, Passive Metashells with Adaptive Thermal Conductivities: Chameleonlike Behavior and Its Origin. *Phys. Rev. Appl.* **11**, 054071 (2019).